Imaging the total wavefields by reflectivity inversion using amplitude-normalized wavefield decomposition: field data example

Alba Ordoñez*, PGS Geophysical AS and University of Oslo, Walter Söllner and Tilman Klüver, PGS Geophysical AS

SUMMARY

Based on an example acquired with dual-sensor towed-streamers and time and depth distributed sources, we image the total up- and downgoing wavefields using primaries and multiples. The imaging framework is based on computing the subsurface impulse response (i.e., reflectivity). At every depth level, the latter can be obtained by inverting the matrix form of an integral equation defined in terms of the amplitude-normalized upgoing pressure and downgoing vertical velocity wavefields. This procedure gives the reflectivity matrix. The total upgoing wavefield used in the imaging scheme is composed of the scattered energy from primaries and multiples. The primary reflected wavefield is generated by a direct downgoing source wavefield, which is mostly passing the acquisition surface at offsets smaller than the nearest data channel. Hence, the most relevant part of the direct wavefield is not measured in the studied example. From the near-field pressure measurements, we predict the missing direct arrivals needed to image the primary reflected wavefield; and we then synthesize the total downgoing wavefield by adding the downgoing scattered energy. By downward extrapolating the total up- and downgoing wavefields, the information of the subsurface is extracted from the reflectivity matrix in the spatial and angular domains.

INTRODUCTION

Classical imaging theory is based on single scattering. The reflected wavefield is defined as an upward travelling wave that only contains primary reflections. The incident wavefield is described by an analytical function or a direct downgoing wavefield. As receiver ghosts and multiples have at least one downward reflection, they generate upgoing reflections in the same way as the direct downgoing wavefield. They can therefore be used as secondary virtual sources to provide additional information of the subsurface.

Many works have shown that by incorporating these secondary virtual sources in the imaging scheme, it was possible to increase the spatial illumination of the subsurface (e.g., Berkhout and Verschuur, 1994; Guitton, 2002; Lameloise and Söllner, 2011; Lu et al., 2011), improve the vertical resolution of the image (e.g., Berkhout and Verschuur, 2006; Muijs et al., 2007), and reduce the acquisition related footprints (e.g., Castillo and Söllner, 2013; Lu et al., 2013).

Dual-sensor towed-streamer (or multicomponent) acquisition allows recording the vertical particle velocity wavefield, along with the pressure wavefield. This offers the perspective to redefine the imaging framework based on up- and downgoing wavefields using primaries and multiples. For example, by adequately combining the up- and downgoing components of the pressure and vertical velocity measurements, we can retrieve the impulse response of the subsurface (e.g., Ordoñez et

al., 2014 and 2016). For complex inhomogeneous media, this impulse response (or reflectivity) can be computed by solving an integral equation in the frequency-space domain (e.g., Amundsen, 2001). This integral equation is defined in terms of the upgoing pressure and the downgoing vertical velocity wavefields. Based on synthetic data, Ordoñez et al. (2016) illustrates how the inversion of the matrix form of this integral equation gives an estimate of the reflectivity matrix. The latter is used to extract information of the subsurface in the spatial and angular domains. In order to suppress wavefield interactions coming from the overburden (i.e., crosstalk), the inversion problem should be well constrained and the distribution of the discretized receivers should represent the complexity of the subsurface. Furthermore, the method requires using the total up- and downgoing wavefields. Both the up- and downgoing wavefields should contain the scattered energy from primaries and multiples; the direct wavefield emitted from the source should also be included for the downgoing wavefield. The most relevant part of the direct wavefield which generates the primary reflected wavefield is close to vertical incidence. In towed-streamer acquisition of field data, this is normally not measured.

Following the reflectivity inversion approach described in Ordoñez et al. (2016), this abstract aims at showing an application of the method on field data. We have chosen a 2D field data example from the Møre Margin High of the Norwegian Sea. It was acquired with dual-sensor towed-streamers, containing collocated pressure and vertical particle velocity sensors (e.g. Tenghamn et al., 2007). The acquisition was also performed with time and depth distributed sources (Parkes and Hegna, 2011).

IMAGING FRAMEWORK

In a small source-free depth interval at the measurement surface, the pressure wavefield P and the vertical velocity wavefield V_z can be decomposed into their up- (U^P, U^{V_z}) and downgoing (D^P, D^{V_z}) components (e.g., Claerbout, 1976; Fokkema and van den Berg, 1993). These decomposed wavefields are referred to as amplitude-normalized separated wavefields. Following Rayleigh's reciprocity theorem, the total upgoing pressure and the downgoing vertical velocity can be related with the following Fredholm integral equation (e.g., Amundsen, 2001; Ordoñez et al., 2014):

$$U^P(\mathbf{x_r}, \mathbf{x_s}) = -2i\omega\rho \int_{\mathbf{x}\in\partial V} R(\mathbf{x_r}, \mathbf{x}) D^{V_z}(\mathbf{x}, \mathbf{x_s}) d^2\mathbf{x}. \quad (1)$$

In equation 1, i is the imaginary unit, ω is the angular frequency and ρ is the mass density. The upgoing wavefield $U^P(\mathbf{x_r}, \mathbf{x_s})$ and the downgoing wavefield $D^{V_z}(\mathbf{x}, \mathbf{x_s})$ have been generated at $\mathbf{x_s}$, and respectively received at $\mathbf{x_r}$ and at $\mathbf{x}$. The reflectivity R relates the downgoing wavefield at $\mathbf{x}$ to the up-

Imaging by reflectivity inversion: field data example

going wavefield at $\mathbf{x_r}$. In practice, only a band-limited reflectivity can be estimated using discretized up- and downgoing wavefields. We can discretize the integral equation 1 into its matrix form and consider multiple sources to constraint the inversion problem. We introduce the filtered downgoing vertical velocity $D_f^{V_z} = -2i\omega\rho D^{V_z}$ and define the matrices $\mathbf{U^P}$, $\mathbf{R}$ and $\mathbf{D_f^{V_z}}$ for different sources (columns) and discretized receivers (rows). The matrix version of the integral equation 1 writes (e.g., Ordoñez et al., 2014):

$$\mathbf{U^P} = \mathbf{R}\mathbf{D_f^{V_z}}. \tag{2}$$

As pointed out by many authors (Berkhout and Verschuur, 2003; Wapenaar et al., 2008; Vasconcelos et al., 2010; Ordoñez et al., 2016), an approximated reflectivity $\mathbf{R}_\lambda \approx \mathbf{R}$ can be obtained, for example, from a regularized least-squares inversion:

$$\mathbf{R}_\lambda = \mathbf{U^P}\mathbf{D_f^{V_z}}^\dagger[\mathbf{D_f^{V_z}}\mathbf{D_f^{V_z}}^\dagger + \lambda^2\mathbf{I}]^{-1}, \tag{3}$$

where λ is the regularization parameter and the superscript $\dagger$ denotes the conjugate transpose. The algorithm used to compute the reflectivity matrix $\mathbf{R}_\lambda$ is independent for each frequency and depth level. We execute the following steps to calculate the reflectivity matrix and extract the information of the subsurface:

1. At the measurement surface: decompose the pressure and vertical velocity wavefields and fill in $\mathbf{U^P}$ and $\mathbf{D_f^{V_z}}$

2. Downward extrapolate in depth the elements of $\mathbf{U^P}$ and $\mathbf{D_f^{V_z}}$

3. Compute the reflectivity matrix $\mathbf{R}_\lambda$ using equation 3:

   - Select the elements on the main diagonal of $\mathbf{R}_\lambda$ and extract the zero-time lag to compute the structural image I: $I(\mathbf{x}) = \sum_\omega R_\lambda(\mathbf{x_r} = \mathbf{x}, \mathbf{x})$

   - Select the non-diagonal elements of $\mathbf{R}_\lambda$ (such as the rows of the matrix) to extract the angle-dependency (e.g., de Bruin et al., 1990; Ordoñez et al., 2016).

TOTAL UP- AND DOWNGOING WAVEFIELDS

The field data was acquired using a time and depth distributed source system, composed of two typical seismic sources. The sources, located at the same horizontal position and at the two distinct depths of 10 and 14 m, were fired with random time delays. At the acquisition level (set to 25 m), dual-sensor towed-streamers composed of collocated hydrophones and geophones recorded pressure and vertical velocity wavefields.

From dual-sensor measurements, the up- and downgoing pressure wavefields can be computed at a horizontal reference level, according to:

$$\widetilde{U^P} = 1/2[\widetilde{P} - (\omega\rho/k_z)\widetilde{V_z}] \tag{4}$$

$$\widetilde{D^P} = 1/2[\widetilde{P} + (\omega\rho/k_z)\widetilde{V_z}], \tag{5}$$

where the superscript $\sim$ indicates transformation to the wavenumber domain. The vertical wavenumber $k_z = \sqrt{(\omega)/c)^2 - k_x^2}$

can be expressed in terms of the horizontal wavenumber k_x and the propagation velocity c. The parameters related to the wavefield separation (i.e., k_z and ρ) are given here at the acquisition level. The source wavefield defined in the imaging framework is the filtered downgoing vertical velocity $D_f^{V_z}$, which can be obtained from the downgoing pressure, according to:

$$\widetilde{D_f^{V_z}} = -2ik_z\,\widetilde{D^P}. \tag{6}$$

A basic summary of how we computed the total up- and downgoing wavefields for imaging the field data example is presented in Figure 1. The total upgoing wavefield was obtained from wavefield separation of scattered pressure and vertical velocity wavefields, which contained primaries and multiples. The total downgoing wavefield was synthesized by adding the contributions of the downgoing scattered wavefield (derived from wavefield separation) and the direct downgoing wavefield. The latter was reconstructed from the notional source signatures, derived from the near-field pressure measurements (e.g., Ziolkowski et al., 1982). In the chosen example, the measured part of this wavefield is beyond 80 degrees already at the nearest channels. The reconstructed direct wavefield contains the near-offset traces that were originally missing in the measurements; these traces constitute a relevant part of the wavefield as they generate the primary reflections.
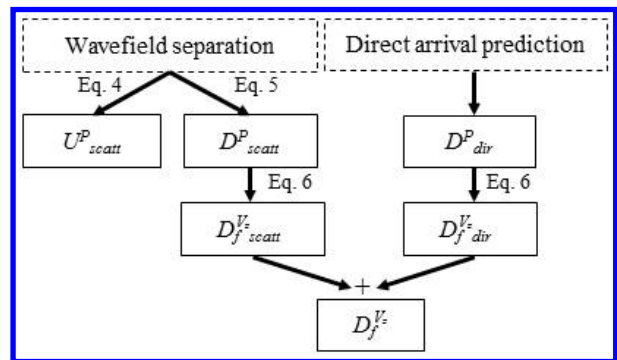

Figure 1: Simplified workflow showing how the total up- and downgoing wavefields were synthesized.
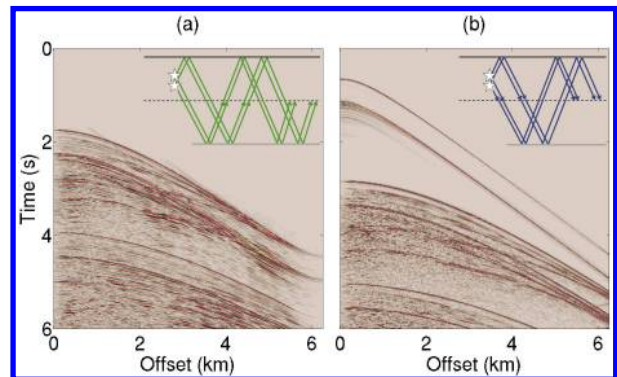

Figure 2: Total up- (a) and downgoing (b) wavefields downward extrapolated in depth.

Imaging by reflectivity inversion: field data example

Figure 2 shows shot records (downward extrapolated in depth) of the synthesized up- (U^P)- and downgoing ($D_f^{V_z}$) wavefields that are used for imaging.

IMAGING RESULTS

We considered a seismic profile consisting of 140 shots spaced at intervals of 50 m (moving from left to right). The receiver interval was 12.5 m and the number of receivers per shot was 500. Within the frequency range from 5 to 60 Hz, we computed the structural image by reflectivity inversion (i.e., by selecting the main diagonal of the zero-time reflectivity). The result is displayed in Figure 3a. The information of the total up- and downgoing wavefields is properly combined in a high-resolution image. Notice that the target area includes a sedimentary section and part of a basalt structure.
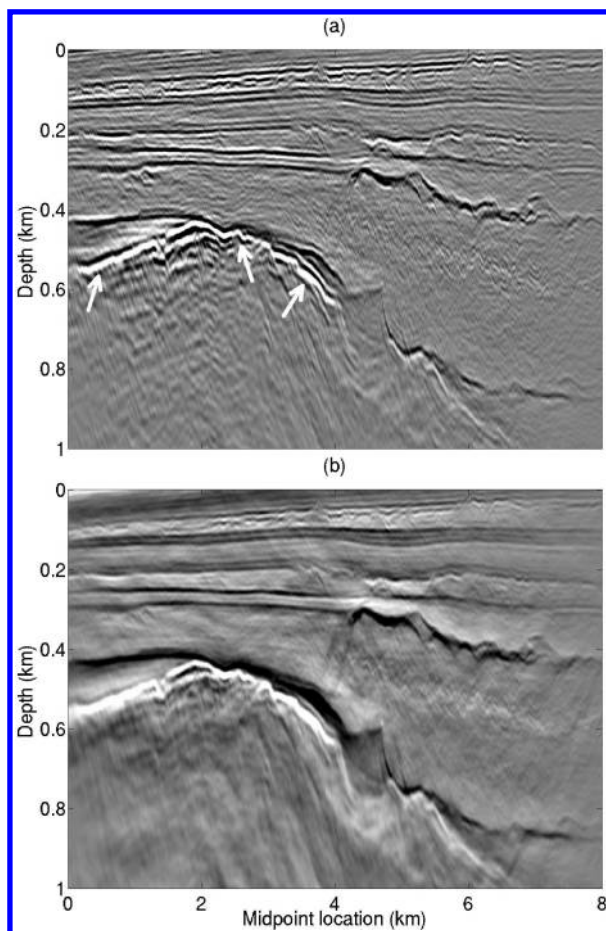

Figure 3: Structural images obtained (a) by reflectivity inversion and (b) by applying the deconvolution imaging condition of equation 7. The white arrows in (a) indicate the top basalt.

To evaluate the overall quality of the result obtained by reflectivity inversion, we computed for comparison, the structural image from the following deconvolution imaging condition (Ordoñez et al., 2014 and 2016):

$$I(\mathbf{x}) = \sum_{\mathbf{x_s}} \sum_{\omega} \frac{U^P(\mathbf{x_r} = \mathbf{x}, \mathbf{x_s}) D_f^{V_z*}(\mathbf{x_r} = \mathbf{x}, \mathbf{x_s})}{\langle D_f^{V_z}(\mathbf{x_r} = \mathbf{x}, \mathbf{x_s}) D_f^{V_z*}(\mathbf{x_r} = \mathbf{x}, \mathbf{x_s}) \rangle + \lambda^2}, \quad (7)$$

where the superscript * denotes complex conjugation. Besides adding to the denominator the stabilization parameter λ, we have also introduced the smoothing operator $\langle \, \rangle$ to prevent even more stability problems (Guitton, 2007). This deconvolution imaging condition can be seen as a special case of the developed inversion approach, assuming that the subsurface points are locally reacting. By this, we mean that the motion of one point only depends on the incident wavefield arriving on this point, and is independent of the motion of any surrounding area. Notice that the result computed from equation 7 (Figure 3b) presents a large amount of long wavelengths, which lead to a lower resolution image compared to Figure 3a.

The structural image of Figure 3a was built by selecting the zero-spatial and temporal lags of the reflectivity matrix. This image only contains an angle-averaged value of each reflector point. By selecting the rows of the monochromatic reflectivity matrices, it is possible to extract information of the subsurface in the angular domain. Based on de Bruin et al. (1990) and Ordoñez et al. (2016), (1) we transform the selected rows from the frequency-space to the frequency-wavenumber domain, (2) we scale the transformed subsets by a source decomposed into plane-waves in order to obtain plane-wave reflection coefficients, (3) we map the obtained plane-wave reflection coefficient from the wavenumber domain to the angle domain, and (4) we compute the zero-time reflection coefficients by summing over frequencies. By following this procedure, we built the angle gathers and the angle-based structural images that are presented in Figures 4 and 5.

The angle gathers of Figure 4 were computed for some receiver locations. Notice that the events become less and less flat as soon as we move into the basalt body. This may indicate that in that region the velocity model used for the extrapolation becomes less accurate.

The angle-based structural images of Figure 5 were obtained by selecting different angle ranges of the zero-time reflection coefficients, and stacking their contributions for each receiver location. These images can be utilized to identify the range of angles contributing to the target illumination. From Figure 5, we observe that between 0 and 40°, the images are consistent in terms of structural information and interface thickness. The high angles (40-60°) mainly provide information about the shallow part of the image, with long wavelengths compared to the near incident angles (0-10°). The main contribution to the basalt structure imaging comes from the angle range of 20-40°. The first shots of the seismic profile lay outside the target imaging area and only part of their one-sided spread contribute to imaging the target. This explains that the near incident angles (0-20°) do not provide information about the left edge of the target. Similarly, only part of the spread of the last shots is inside the target imaging area, that is why the high angles (40-60°) do not image the right edge of the target.

Imaging by reflectivity inversion: field data example
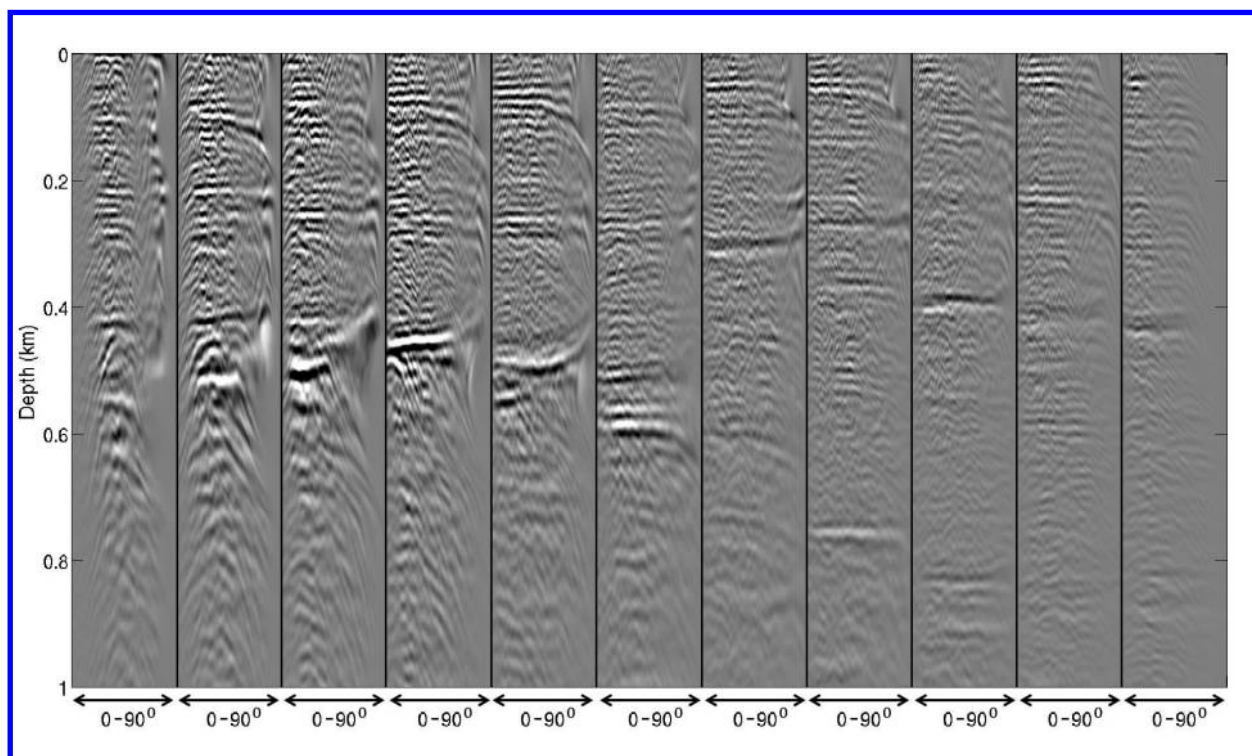
Figure 4: Angle gathers obtained for some receiver locations
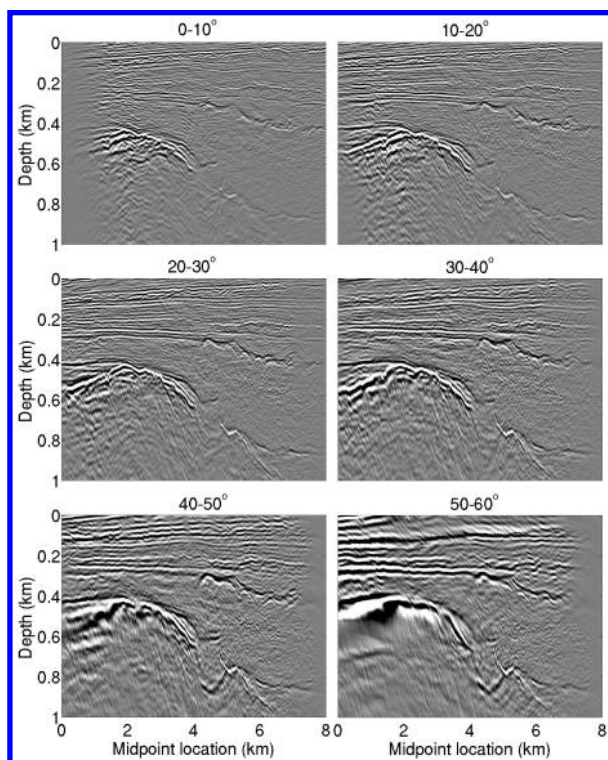

Figure 5: Angle-based structural images obtained by stacking the contributions of different angle ranges.

CONCLUSIONS

This study illustrates on a field data example, different imaging results obtained by reflectivity inversion. The total receiver wavefield composed of the upgoing scattered energy from primaries and multiples was used for imaging. Regarding the source wavefield, we synthesized a total downgoing wavefield composed of the direct arrival wave and the downgoing scattered wavefield. The near-field pressure measurements were used for predicting the direct wavefield at the offsets corresponding to the measurements, but also at the near-offset channels that were originally missing in the acquired direct arrival. This information was necessary to adequately image the primary reflected wavefield. The downgoing scattered wavefield derived from wavefield separation of dual-sensor towed-streamer measurements added the contribution of secondary virtual sources. The reflectivity inversion approach combined the information from the total up- and downgoing wavefields to image and characterize the subsurface in the spatial and angular domains.

ACKNOWLEDGMENTS

REFERENCES

Amundsen, L., 2001, Elimination of the free-surface-related multiples without need of the source wavelet: Geophysics, **66**, 327–341, http://dx.doi.org/10.1190/1.1444912.

Berkhout, A. J., and D. J. Verschuur, 1994, Multiple technology: Part 2, migration of multiple reflections: 64th Annual International Meeting, SEG, Expanded Abstracts, 1497-1500, http://dx.doi.org/10.1190/1.1822821.

Berkhout, A. J., and D. J. Verschuur, 2003, Transformation of multiples into primaries reflections: 73rd Annual International Meeting, SEG, Expanded Abstracts, 1925-1928, http://dx.doi.org/10.1190/1.1817697.

Berkhout, A. J., and D. J. Verschuur, 2006, Imaging of multiple reflections: Geophysics, **71**, no. 4, SI209–SI220, http://dx.doi.org/10.1190/1.2215359.

Castillo, C., and W. Söllner, 2013, 3D shallow target imaging from separated wavefields: 75th Annual International Conference and Exhibition, EAGE, Extended Abstracts, We 02 06.

Claerbout, J. F., 1976, Fundamentals of geophysical data processing: McGraw-Hill.

de Bruin, C. G. M., C. P. A. Wapenaar, and A. J. Berkhout, 1990, Angle-dependent reflectivity by means of prestack-migration: Geophysics, **55**, 1223–1234, http://dx.doi.org/10.1190/1.1442938.

Fokkema, J. T., and P. M. van den Berg, 1993, Seismic applications of acoustic reciprocity: Elsevier Science Publishing Co., Inc.

Guitton, A., 2002, Shot-profile migration of multiple reflections: 72nd Annual International Meeting, SEG Expanded Abstract, 1296–1299, http://dx.doi.org/10.1190/1.1816892.

Guitton, A., A. A. Valenciano, D. Bevc, and J. Claerbout, 2007, Smoothing imaging condition for shot-profile migration: Geophysics, **72**, no. 3, S149–S154, http://dx.doi.org/10.1190/1.2712113.

Lameloise, C., and W. Söllner, 2011, Shallow target depth imaging from separated wavefields: 73rd Annual Conference and Exhibition Meeting, EAGE, Extented Abstracts, G007.

Lu, S., N. D. Whitmore, A. A. Valenciano, and N. Chemingui, 2011, Imaging of primaries and multiples with 3D SEAM synthetic: 81st Annual International Meeting, SEG, Expanded Abstracts, 3217–3221, http://dx.doi.org/10.1190/1.3627864.

Lu, S., N. D. Whitmore, H. LeGleut, and A. Long, 2013, 3D high-resolution imaging using separated wavefields, 75th Annual Conference and Exhibition Meeting, EAGE, Extended Abstracts, Th 08 09.

Muijs, R., J. O. A. Robertsson, and K. Holliger, 2007, Prestack depth migration of primary and surface-related multiple reflections: Part I — Imaging: Geophysics, **72**, no. 2, S59–S69, http://dx.doi.org/10.1190/1.2422796.

Ordoñez, A., W. Söllner, T. Klüver, and L. J. Gelius, 2014, Migration of primaries and multiples using an imaging condition for amplitude-normalized separated wavefields: Geophysics, **79**, no. 5, 1–14, http://dx.doi.org/10.1190/geo2013-0346.1.

Ordoñez, A., W. Söllner, T. Klüver, T., and L.J. Gelius, 2016, Subsurface reflectivity estimation from imaging of primaries and multiples using amplitude-normalized separated wavefields: Geophysics, accepted for publication.

Parkes, G., and S. Hegna, 2011, An acquisition system that extracts the earth response from seismic data: First Break, **29**, 81–87.

Tenghamn, R., S. Vaage, and C. Borresen, 2007, A dual-sensor, towed marine streamer: its viable implementation and initial results: 77th Annual International Meeting, SEG, Expanded Abstracts, 989–993, http://dx.doi.org/10.1190/1.2792571.

Vasconcelos, I., P. Sava, and H. Douma, 2010, Nonlinear extended images via image-domain interferometry: Geophysics, **75**, no. 6, SA105–SA115, http://dx.doi.org/10.1190/1.3494083.

Wapenaar, K., E. Slob, and R. Snieder, 2008, Seismic and electromagnetic controlled-source interferometry in dissipative media: Geophysical Prospecting, **56**, 419–434, http://dx.doi.org/10.1111/j.1365-2478.2007.00686.x.

Ziolkowski, A., G. Parkes, L. Hatton, and T. Haugland, 1982, The signature of an air gun array: Computation from near-field measurements including interactions: Geophysics, **47**, 1413–1421, http://dx.doi.org/10.1190/1.1441289.